Journal of Energy Chemistry 53 (2021) 241–250

Contents lists available at ScienceDirect

Journal of Energy Chemistry

journal homepage: www.elsevier.com/locate/jechem

Unraveling and optimizing the metal-metal oxide synergistic effect in a highly active $Co_x(CoO)_{1-x}$ catalyst for CO_2 hydrogenation

Kun Zhao [a,b,*], Marco Calizzi [a,b], Emanuele Moioli [a,b], Mo Li [a,b], Alexandre Borsay [a,b], Loris Lombardo [a,b], Robin Mutschler [a,b], Wen Luo [a,b,*], Andreas Züttel [a,b]

[a] Laboratory of Materials for Renewable Energy, Institute of Chemical Sciences and Engineering, École Polytechnique Fédérale de Lausanne (EPFL), 1951 Sion, Switzerland
[b] Swiss Federal Laboratories for Materials Science and Technology (EMPA), 8600 Dübendorf, Switzerland

ARTICLE INFO

Article history:
Received 1 April 2020
Revised 7 May 2020
Accepted 12 May 2020
Available online 19 May 2020

Keywords:
Cobalt and cobalt oxide
Reactivity
CO_2 hydrogenation
Active site
Adsorption
Activation energy

ABSTRACT

The relation between catalytic reactivities and metal/metal oxide ratios, as well as the functions of the metal and the metal oxides were investigated in the CO_2 hydrogenation reaction over highly active $Co_x(CoO)_{1-x}$ catalysts in operando. The catalytic reactivity of the samples in the CO_2 methanation improves with the increased CoO concentration. Strikingly, the sample with the highest concentration of CoO, i.e., $Co_{0.2}(CoO)_{0.8}$, shows activity at temperatures lower than 200 °C where the other samples with less CoO are inactive. The origins of this improvement are the increased amount and moderate binding of adsorbed CO_2 on CoO sites. The derivative adsorption species are found to be intermediates of the CH_4 formation. The metallic Co functions as the electronically catalytic site which provides electrons for the hydrogenation steps. As a result, an abundant amount of CoO combined with Co is the optimal composition of the catalyst for achieving the highest reactivity for CO_2 hydrogenation.

1. Introduction

CO_2 conversion to hydrocarbons has received enormous attention in the past decade for the possibilities of exploiting CO_2 as feedstock in the storage of sustainable energy and of closing the carbon cycle. Metal oxides-supported transition metals such as Fe, Co, Ni, Cu and Ru have been studied as effective catalysts in the CO_2 hydrogenation reaction. The main products of the reaction over the above-mentioned catalysts at atmospheric pressure are CH_4 and CO [1–5].

In general, CO_2 hydrogenation catalysts are prepared in the form of supported metal particles. The metal site is considered as the reactive center while the support is used for dispersing and stabilizing the metal nanoparticles [6,7]. However, recent studies showed that the support could also have an important role in the heterogeneous catalysis of carbon-related reactions. In methanol synthesis from CO_2 and H_2 on Cu-based supported catalysts, the ZrO_2 support facilitates the moderate bindings of the key reaction intermediates at the interface of Cu and ZrO_2 [8,9]. Moreover, different supports lead to different key intermediates of methanol production, e.g., TiO_2 and ZnO_2 support surfaces produce formate intermediate, while ZrO_2 support surface forms CO*, HCO*, and H_2CO^* intermediates. The formate intermediate is less active for methanol formation compared to the other intermediates, resulting in a less active catalyst with TiO_2 support [10–12]. In higher alcohol synthesis from syngas over Co/CeO_2 catalyst, the CeO_2 support functions for dispersing the Co nanoparticles. However, the Co is partially oxidized into CoO_x due to the strong metal-support interactions. This results in an active Co-CoO_x pair for the higher alcohol synthesis where the Co site accounts for CO dissociation to form CH_x species and the CoO_x site accounts for CO undissociated activation to form CH_xO^* species. These CH_x and CH_xO^* species combine to form higher alcohol at the interface of Co and CoO_x [13]. In CO_2 and CO hydrogenation reaction, the partially cobalt nanoparticles on TiO_2 supports, $Co/CoO/TiO_2$, exhibit higher CO_2 and CO conversion rate than the metallic Co/TiO_2, indicating CoO improves reactivity of the catalyst either by the component itself or by forming active interface with the metal or with the support. However, changing the TiO_2 support to SiO_2 support reversed the activity, implying that different support varies the activity of the catalyst [14]. An early work from Somorjai and co-workers claimed a promotion effect of oxide on Rh metal surface for the CO and CO_2 hydrogenation [15]. The promotion effect was attributed to the

* Corresponding authors at: Laboratory of Materials for Renewable Energy, Institute of Chemical Sciences and Engineering, École Polytechnique Fédérale de Lausanne (EPFL), 1951 Sion, Switzerland.
E-mail addresses: kun.zhao@epfl.ch (K. Zhao), wen.luo@epfl.ch (W. Luo).

https://doi.org/10.1016/j.jechem.2020.05.025

high Lewis acidity of the metal cations of the oxide by the possible function of cleavage of the C–O bond at the interface of Rh/oxide for CH_4 formation. Therefore, they suggested the support participated in the catalytic reaction via cleaving chemical bonds, but this was still disputable. Recent work using supports from Lewis acidic to basic properties to study the support effects in Fischer-Tropsch reaction demonstrated a volcano relation between the reaction rate and Lewis acid-base nature of the support, where the supports was not considered to be catalytic active [16].

The above-mentioned arguments on the role of the support motivate us to clarify the role of the support in the CO_2 hydrogenation reaction, and the relation between the combinations of metal and support and their catalytic reactivity, as these are important for the design of efficient catalysts for CO_2 conversion. In our previous study on a Ru/Al_2O_3 catalyst, we found that CO_2 adsorbed initially on the Al_2O_3 surface and on the interface of Al_2O_3 and Ru. Then the adsorbed CO_2 and its derivative species migrate to the Ru atoms for the subsequent hydrogenation steps. The support itself did not provide a site for the CO_2 hydrogenation steps [17,18]. Herein, we hypothesized that there might be an optimized metal to metal oxide ratio for the highest reactivity toward CO_2 hydrogenation.

To explore this hypothesis we would like to synthesize catalysts with varying fractions of metal and support for CO_2 hydrogenation. However, a "foreign" support could create multiple interfaces, i.e. metal/metal oxide interface, metal/support interface, metal oxide/support interface due to strong metal-support interaction, and this would make it difficult to explore cleanly the effect of the metal/metal oxide ratio [19–22]. To avoid this complexity and to vary only the metal/oxide ratio, we designed a "self-supported" cobalt catalyst with different ratios of the metallic Co and the CoO, i.e., $Co_x(CoO)_{1-x}$ with $0 < x < 1$.

Herein, we developed an in operando reduction method to synthesize the $Co_x(CoO)_{1-x}$ samples and to analyze the CO_2 hydrogenation reaction in continuous experiments on one platform: a diffuse reflectance infrared Fourier transform spectroscopy-mass spectroscopy-gas chromatograph (DRIFTS-MS-GC) instrument, previously described [23]. The molar concentrations of Co were quantified using the H_2 consumption from the MS data. To verify this in situ quantification, X-ray photoelectron spectroscopy (XPS) was applied to analyze the compositions and the ratios of Co content in the catalysts. Subsequently, the reactivity of these $Co_x(CoO)_{1-x}$ samples in the CO_2 hydrogenation reaction was investigated in the DRIFTS-MS-GC instrument. The gas phase and catalyst surface were observed simultaneously to unravel the reaction mechanisms. To understand the origins of the different reactivities, we analyzed the gas–surface interaction using temperature-programmed desorption–mass spectroscopy (TPD-MS). Additionally, surface electronic structures of these samples were measured using near ambient-pressure X-ray photoelectron spectroscopy (NAP-XPS) to check whether the oxide creates special electronic states for the catalysis.

The specific purpose of this work is to answer three key scientific questions: (1) What is the optimal ratio of metal/metal oxide to achieve the highest reactivity in CO_2 hydrogenation? (2) Is the role of the support simply to disperse the metal nanoparticles or does it have a direct role in the reaction? (3) If there is a direct role, is it only to provide adsorption sites for CO_2 and the associated adsorbed species, or also to provide electronically active sites that reduce those adsorbed species to hydrocarbons?

We found that the reactivity of the samples depended strongly on the Co/(Co + CoO) molar ratio. Importantly, we produced a catalyst that is highly active at low reaction temperature. The catalyst with a higher concentration of CoO has a lower onset reaction temperature, a lower activation energy of CH_4 formation, and a higher CO_2 conversion. We demonstrate that the improved activity of the catalyst stems solely from the role of CoO in providing sites for CO_2 adsorption and lowering the CO_2 binding energy, but not in providing active sites for the hydrogenation reaction.

2. Experimental

2.1. Sample preparation

The samples were prepared by starting with Co_3O_4 and then reducing this material in H_2 at various temperature/time profiles to produce several self-supported catalysts with controlled ratios of Co and CoO, $Co_x(CoO)_{1-x}$ ($0 < x < 1$). Co_3O_4 was obtained by calcination of $Co(NO_3)_2{\cdot}6H_2O$ (Sigma-Aldrich, 98%) at 300 °C for 12 h followed by a temperature ramp of 2 °C min^{-1} to 400 °C and then continued calcination for 2 h at 400 °C.

To determine the temperature required for reducing Co_3O_4, the reduction process was tracked with a microbalance (Rubotherm, Germany). Typically, 160 mg of Co_3O_4 was loaded in the microbalance and a gas flow mixture of 30 mL min^{-1} H_2 and 45 mL min^{-1} He at 1 bar was supplied 3 h before the reduction to remove the air. A heating ramp of 2 °C min^{-1} from 25 °C to 400 °C was then applied and the mass loss due to reduction was monitored with an accuracy of 1 μg.

$Co_x(CoO)_{1-x}$ ($0 < x < 1$) catalyst synthesis. The actual catalyst samples used in this study were prepared by reduction of Co_3O_4 in the reaction chamber (HVC, Harrick Scientific) of a DRIFTS instrument (Bruker Tensor 27) in a mixture of H_2/He (flow rate 6 mL min^{-1}/4-mL min^{-1}). Control of the reduction temperature and time allowed us to obtain samples with different Co ratios in a reproducible manner. During reduction, the pressure in the chamber was kept constant at 1 bar by a back pressure valve installed at the exhaust side of the reaction chamber. A quadrupole mass spectrometer (MS, Pfeiffer OmniStar 320) was connected with the DRIFTS reaction chamber to analyze the composition of reactant and product gases using a Faraday detector.

2.2. Characterization

MS meaurements. The amount of H_2 consumed during the reduction was determined by MS analysis. This allowed us to quantify the removal of O atoms from Co_3O_4 during the reduction process and thus obtain the bulk composition of the catalyst.

XPS core level measurements. To quantify the fraction of metallic cobalt on the surface of the $Co_x(CoO)_{1-x}$ catalysts, samples were transferred to the XPS through a glovebox to avoid surface oxidation by the air. The XPS is equipped with a dual anode X-ray source and a Phoibos 100 (SPECS GmbH) hemispherical energy analyzer. The Mg K_α (1253.6 eV) source was used for this study. The survey scan and narrow scan were collected at 90 eV and 20 eV pass energy, respectively. The oxidation states of partially oxidized Co samples were deconvoluted using CasaXPS software. Separate measurements of Co, CoO and Co_3O_4 were used to provide the standard peaks used for the deconvolution.

NAP-XPS valence band measurements. In addition to the core level XPS spectra, we performed measurements of the valence band to probe which components of our samples are catalytically active. The above XPS instrument did not have sufficient resolution for this purpose. Instead, we used a NAP-XPS (SPECS GmbH) instrument. An Al K_α (1486.6 eV) monochromatic X-ray source and a Phoibos 150 NAP hemispherical energy analyzer were used. Survey scans were taken with 50 eV pass energy and narrow scans with 10 eV pass energy. Unfortunately, we could not transfer the samples to this system without exposure to air. To overcome this difficulty we reduced air exposed sample in-situ in the NAP-XPS using H_2. This allowed us to study partially reduced samples and

measure the valence band of the Co and CoO components. The details of this procedure are given in Section 3.6.

N_2 adsorption-desorption isotherm. The specific surface areas were evaluated using a BELSORP mini system (MicrotracBEL Corp., Japan) by nitrogen adsorption–desorption isotherms at 77 K, and was calculated by the Brunauer–Emmet–Teller (BET) method from the built-in software. The empty tube was measured at the same time of the measurements of the samples in order to eliminate the dead volume. The results were listed in Table 1. As we obtained small values of BET surface areas, we measured the nitrogen adsorption-desorption isotherm again in another instrument, Micromeritics Tristar 3000, to be sure of the obtained values. The CO_2 adsorption-desorption isotherm was measured as well at room temperature using Micromeritics Tristar 3000 instrument for evaluating the CO_2 adsorption amount. The BET surface areas and CO_2 adsorption amounts from the Micromeritics Tristar 3000 instrument were listed in Table S1. As the samples were transferred through a glovebox, no activation was applied before the measurements. The accuracies of the measurements were 0.01 $cm^2\ mg^{-1}$.

TEM. The morphology of the samples was visualized in TEM (FEI Tecnai Spirit microscope) operating at 120 kV. The ultrasonic dispersion in ethanol was applied for the sample preparation. The dispersed samples with ethanol were dropped onto the TEM carbon/copper grids and dried in air.

2.3. CO_2 hydrogenation

CO_2 hydrogenation reaction on $Co_x(CoO)_{1-x}$ samples was carried out in an operando surface–gas analysis system. The reactor is a DRIFTS reaction chamber, which at the inlet is connected to a mass flow controller system, and at the outlet is connected to an MS and GC (SRI 8610C). The GC was equipped with a flame ionization detector (FID) and a thermal conductivity detector (TCD). This setup allows gathering surface information by DRIFTS while quantifying the gases by MS and GC. For CO_2 hydrogenation reaction, typically, a $Co_x(CoO)_{1-x}$ sample (160 mg) was compressed into a pellet with 4 mm high and 6 mm diameter. In general, the inlet gas was a mixture of CO_2/H_2/He with flow rates of 1.5 mL min^{-1}/6 mL min^{-1}/4 mL min^{-1}, respectively, at 1 bar. The reaction temperature was programmed from 20 to 350 °C at a heating rate of 2 °C/min. The background of the infrared spectra was taken on the as-reduced sample surface (or 3 h of H_2/He flushed surface for Co_3O_4) in H_2/He flow at room temperature. The infrared spectra were collected every 10 min with spectroscopic resolution of 2 cm^{-1}. The MS determined the mass range of 0–50 amu with a rate of 0.5 s per mass unit. The GC took 9 min for each spectrum, with a cooling interval of 4 min between each scan.

2.4. CO_2 + H_2 adsorption

CO_2 + H_2 co-adsorption on the samples at room temperature was measured with TPD-MS in a flow gas condition where He was used as the carrier gas. The experimental steps include: (1) Co_3O_4 sample was loaded in a quartz tube in air and reduced in H_2/He flow (6 mL min^{-1}/4 mL min^{-1}) in TPD-MS to obtain the fresh $Co_x(CoO)_{1-x}$ sample; (2) the as-prepared $Co_x(CoO)_{1-x}$ sample was flushed by He for one hour; (3) 10 mL min^{-1} CO_2 and 10 mL min^{-1} H_2 gases were applied for 20 min; (4) He flush for at least 40 min to remove the gas phase CO_2 and H_2; (5) heating started to trigger the desorption. The working pressure on the sample was 1 bar. The spectra were taken using a Faraday detector at heating rates of 5, 10, 15, 25, and 40 °C min^{-1}.

3. Results and discussion

3.1. Sample synthesis and characterization

It is generally accepted that the reduction of Co_3O_4 proceeds in a two-step process: Co_3O_4 to CoO, and CoO to Co. However, the reduction temperature of each step is strongly influenced by the properties of Co_3O_4 [13,24–27]. To determine the reduction process of our Co_3O_4 sample, a microbalance was used to monitor the weight loss during the reduction. As shown in Fig. 1, the mass loss shows that Co_3O_4 starts to be reduced at around 200 °C. Until 300 °C, approximately 7% mass loss can be observed, indicating the removal of one oxygen atom per Co_3O_4 molecule to form CoO. Above 300 °C, the slope of the mass loss curve increases and finally the mass loss reaches a plateau of 27% at 370 °C, which can be ascribed to the complete reduction of Co_3O_4 to metallic cobalt. This analysis demonstrates that through controlling the reduction temperature and the reduction time, we can obtain samples with different extents of partially reduced Co.

Using the microbalance results as a guidance to find the temperature to use for reduction, we prepared the catalyst samples in situ in the DRIFTS reaction chamber. This avoided exposing the samples to air before running reactions. We produced three $Co_x(CoO)_{1-x}$ samples at different conditions. The amount of reduced Co in each sample was determined by quantifying the H_2 consumed during the reduction. Details on the experimental procedures are given in Section S1 and Fig. S1. The method of preparation was very reproducible as shown in Fig. S2. Table 1 summarizes the results of the sample preparation for three sets of temperature-time processing conditions. The table gives the Co/(Co + CoO) ratios as determined by hydrogen consumption from the MS analysis as well as data on this ratio obtained by XPS and surface area determined by BET. It is clear that higher reduction temperatures lead to a higher fraction of reduced Co. The reduction time at a given temperature was chosen to obtain a stable ratio of Co/(Co + CoO). XRD patterns of $Co_x(CoO)_{1-x}$ also confirm the reduction of Co_3O_4 to metallic cobalt and CoO (Fig. S3).

Further verification of the oxidation states of $Co_x(CoO)_{1-x}$ was given by XPS measurements via air-free transfer of the samples from the DRIFTS chamber to a glovebox attached to the XPS. As shown in Fig. 2, the as-prepared Co_3O_4 sample shows typical non-symmetric $2p_{3/2}$ and $2p_{1/2}$ peaks at 780.0 and 795.1 eV, respectively, with additional weak satellite peaks, confirming that the surface composition is Co_3O_4. The $Co_x(CoO)_{1-x}$ samples were deconvoluted with standard Co and CoO spectra, where the $2p_{3/2}$ and $2p_{1/2}$ peaks of metallic cobalt located at 778.7 and 793.7 eV, respectively, and those of CoO located at 781.1 and 796.8 eV. The ratios of the peak areas showed that the fractions of Co were 19%, 51%, and 75% for the three $Co_x(CoO)_{1-x}$ samples. The slight difference in the value of Co fraction compared to the results calcu-

Table 1
H_2 reduction conditions, metal ratios and specific surface areas of $Co_x(CoO)_{1-x}$ samples.

Sample	H_2 reduction conditions	Co/(Co + CoO) ratio from MS	Co/(Co + CoO) ratio from XPS	BET surface area ($m^2\ g^{-1}$)
Co_3O_4	N/A	0	0	18.59
$Co_{0.2}$	200 °C 10 h	0.16 ± 0.01	0.19	13.92
$Co_{0.5}$	300 °C 5 h	0.57 ± 0.05	0.51	5.62
$Co_{0.8}$	400 °C 4 h	0.79 ± 0.04	0.75	2.09

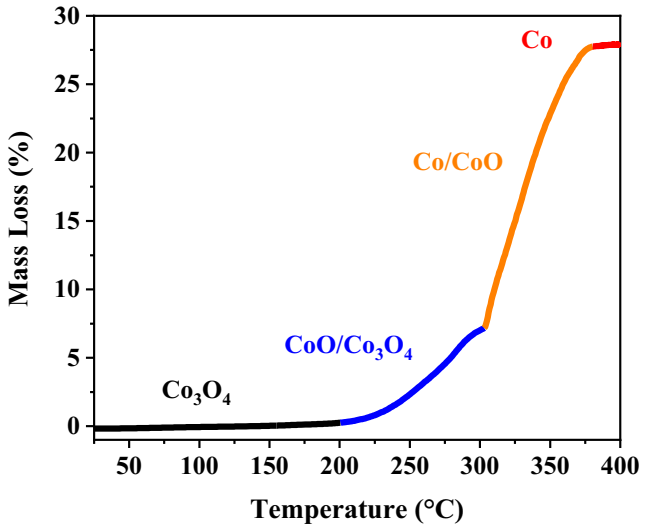

Fig. 1. Mass loss of Co_3O_4 sample when reduced in H_2/He flow with a heating rate of 2 °C min^{-1} in a microbalance.

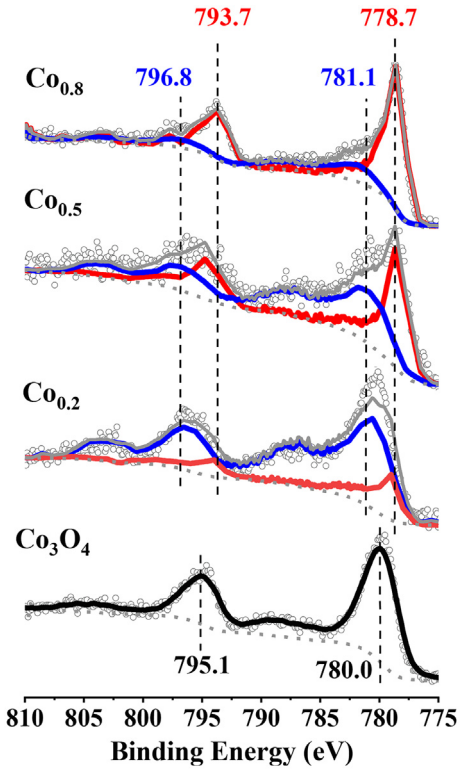

Fig. 2. XPS of Co $2p_{3/2}$ and $2p_{1/2}$ peaks of synthesized samples. Black, blue and red lines represent the deconvoluted signals of Co_3O_4, CoO and Co states, respectively. Gray and gray dash lines are the total fitted spectra and baseline, respectively. The peaks were fitted by using the standard spectra of Co_3O_4, CoO and Co.

lated from H_2 consumption is likely due to that XPS is surface sensitive while H_2 consumption is bulk sensitive. Referring to the quantifications from both XPS and H_2 consumption, we name the samples as $Co_{0.2}$, $Co_{0.5}$, and $Co_{0.8}$.

The morphology of the samples was visualized using TEM. As shown in Fig. 3, all four samples show elongated particle shape and the particle width increases from 20 to 100 nm along with increasing metallic cobalt concentration. The increased particle size originates from the sintering of metallic cobalt through high

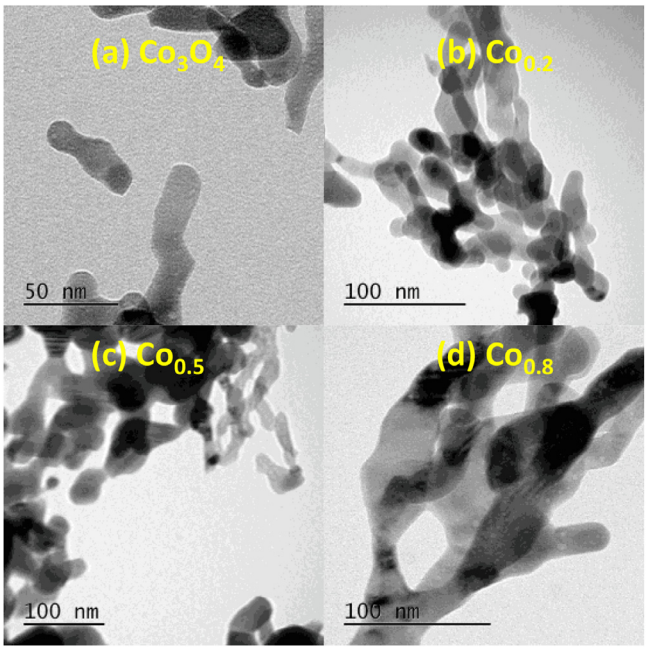

Fig. 3. TEM of prepared samples. (a) Co_3O_4, (b) $Co_{0.2}$, (c) $Co_{0.5}$, (d) $Co_{0.8}$.

temperature reduction treatment. BET measurements were used for evaluating the specific surface area (Table 1). In agreement with the TEM image, the specific surface area decreases with the increased ratio of metallic cobalt.

3.2. Activity in the CO_2 conversion

The activities of the $Co_x(CoO)_{1-x}$ samples for the CO_2 hydrogenation reaction were evaluated in the DRIFTS chamber under a CO_2/H_2/He gas flow with a programmed temperature ramp. To check the reactivity of the samples in a wide temperature range, we heated the reaction chamber from room temperature up to a high temperature of 350 °C. Fig. 4(a) shows the CO_2 conversion, as measured by the consumption of CO_2, as a function of reaction temperature. The trend of CO_2 conversion over the different samples is in the order $Co_{0.2}$ > $Co_{0.5}$ > $Co_{0.8}$ > Co_3O_4 at any given temperature below 280 °C. For instance, 63%, 53%, and 23% CO_2 are converted at 250 °C on $Co_{0.2}$, $Co_{0.5}$, and $Co_{0.8}$ samples, respectively. The CO_2 conversion reaches highest value with 98%, 99%, and 93% at 350 °C on $Co_{0.2}$, $Co_{0.5}$, and $Co_{0.8}$ samples, respectively. The reason of the similar high conversion at this high temperature could be that the reaction approaches the thermodynamic limit. The same trend was found in the yield of the main product CH_4 (Fig. S4). The yields are commensurate as the CO_2 conversion. For comparison, the conversions obtained here are higher than the conversions on the commercial 0.5 wt% Ru/Al_2O_3 catalyst at the same applied pressure at 1 bar and space velocity at 5300 h^{-1} as in this work [3]. The maximum conversion of CO_2 on that Ru/Al_2O_3 is reported to be 75% and at 380 °C, where 75% conversion is found at 260 °C on our $Co_{0.2}$ sample. These conversions are also much higher than the reported <60% CO_2 conversion on the 3% Ru/Al_2O_3 and 20% Ni/Al_2O_3 samples at the temperature of 350 °C and space velocity of 55000 h^{-1} [28]. The details of CO_2 conversion, CH_4 yield, CH_4 selectivity, and CH_4 production rate per surface area via normalizing with BET surface area at 200, 225, 250, 275, 300, 325, and 350 °C are showed in Section S3 Fig. S5. The CO_2 conversion and CH_4 yield and selectivity have similar trends as the CO_2 conversion profile shown in Fig. 4(a). The CH_4 production rate

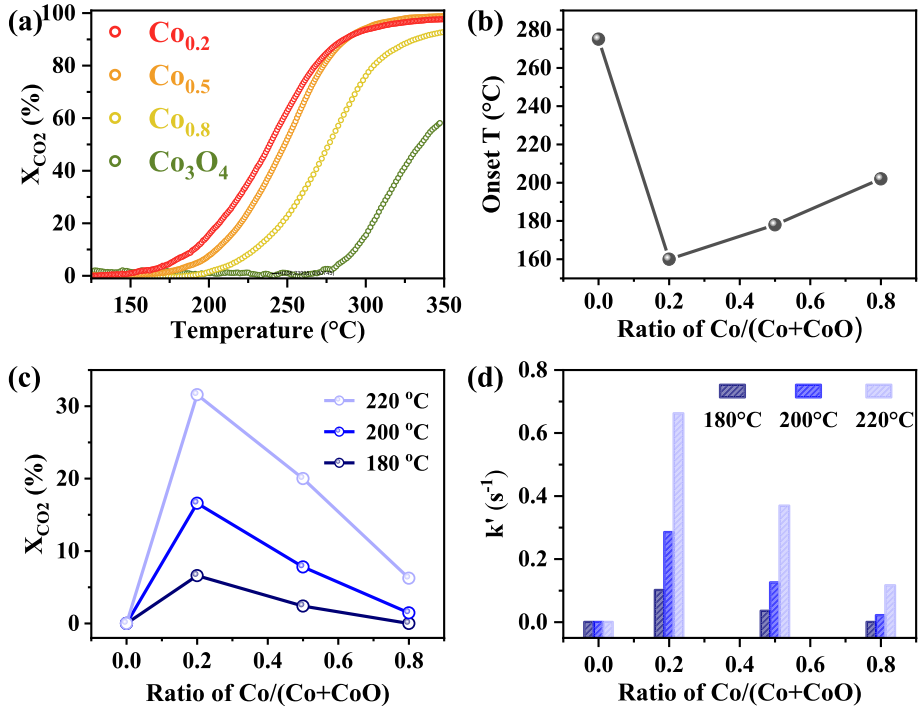

Fig. 4. (a) CO_2 conversion as a function of temperature, (b) onset temperature of 2% CO_2 conversion, (c) CO_2 conversion at 180, 200, and 220 °C, and (d) CH_4 production rates at 180, 200, and 220 °C over the Co_3O_4, $Co_{0.2}$, $Co_{0.5}$ and $Co_{0.8}$ samples.

per surface area inverts this trend, plausibly indicating that the Co is the location where the hydrogenation step takes place.

In addition, we tested the reactivity of the $Co_{0.2}$ sample for long-time CO_2 hydrogenation reaction (Fig. S6). We found that the CO_2 conversion to CH_4 remains stable above 80% after 3 days in stream, demonstrating the sample is long-time active. Therefore, the $Co_x(CoO)_{1-x}$ samples are highly active and efficient for the Sabatier reaction. The differences in the reactivity of these partially reduced samples imply a dependence on the initial state of the catalysts, although the samples could have been further reduced at the high reaction temperature. We believe the reactivity of the Co_3O_4 sample at high temperature is due to some limited partial reduction of this sample in the CO_2/H_2/He gas flow.

Strikingly, these partially reduced samples are quite active at low temperatures. The onset temperatures of CO_2 conversion (2% conversion) increase in the order $Co_{0.2}$ < $Co_{0.5}$ < $Co_{0.8}$ < Co_3O_4, at temperatures of 160, 178, 202, and 275 °C, respectively (Fig. 4 (b)). We compared the CO_2 conversion extent at temperatures of 180, 200, and 220 °C on these samples. As shown in Fig. 4(c), $Co_{0.2}$ sample shows activity at 180 °C while the other samples are not active at this low temperature. $Co_{0.2}$ sample converts 16% and 31% CO_2 at 200 and 220 °C, respectively at the applied space velocity of 5300 h^{-1}. Note that decreasing the space velocity will increase the conversion. These conversions are higher than those on all the rest of the samples at the same temperatures. These results verify our hypothesis that there is an optimal ratio of metal/metal oxide to obtain the highest reactivity toward CO_2 hydrogenation.

The rate constants of CH_4 production were calculated with the assumption of an overall first-order reaction of CO_2 to CH_4 [28–32]. As shown in Fig. 4(d), the highest rate constant occurs on $Co_{0.2}$ sample at the given temperatures, and decreases gradually when the metallic cobalt concentration increases (excluding the Co_3O_4 sample).

Small amounts of CO and C_2H_6 were also detected by MS and GC, and GC data were used to quantify the yield (Fig. S7). The maximum yield of C_2H_6 increases for samples with increasing Co/(Co + CoO) ratio, opposite to CH_4 yield (Fig. S8). C_2H_6 yield is around five-fold larger than CO yield on $Co_x(CoO)_{1-x}$ samples, but threefold lower than CO yield on Co_3O_4 (Fig. S7). These results suggest that C_2H_6, generated through carbon chain growth, is preferably produced on the samples with high Co concentration. Hence, the metallic site, instead of the oxide site, is responsible for the carbon-carbon coupling. This is in agreement with results for the Fischer–Tropsch reaction where metallic cobalt is the active site for carbon chain growth [33]. On the other hand, pure Co_3O_4 surface produces more CO than C_2H_6, suggesting that a reversed-water-gas-shift reaction is more favorable than the carbon-carbon coupling on the pure oxide surface.

The activation energy of CH_4 production, $E_a^f(CH_4)$, was determined using the Arrhenius equation. Details of the calculations based on the measured MS data are given elsewhere [23]. Fig. 5 shows the Arrhenius plot and the values of $E_a^f(CH_4)$. The $E_a^f(CH_4)$ over the samples increases in the order of $Co_{0.2}$ < $Co_{0.5}$ < $Co_{0.8}$ < Co_3O_4. Thus, we see that samples with lower activation energies have lower onset reaction temperatures and higher CO_2 conversions before approaching to the thermodynamic limit.

3.3. Sample stability during hydrogenation

As the CO_2 hydrogenation environment is highly reductive, there is an issue of the stability of the samples during the hydrogenation reaction. For temperatures well below those used to prepare the samples, we are confident that the composition is stable, since the preparation reaction was run long time enough for the composition to reach a constant value as confirmed by the ceasing in hydrogen consumption (Fig. S1). Hence, the measurements of onset temperatures for the reaction (Fig. 4(a, b)) and reaction rate at low temperatures (Fig. 4(c, d)) should correspond to the initial compositions of the samples.

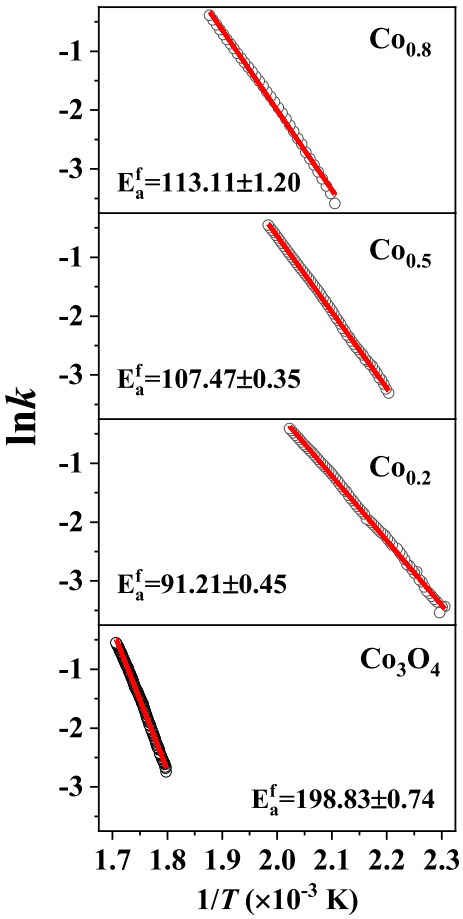

Fig. 5. Arrhenius plot of CH_4 formation in the CO_2 conversion range of 2%–30% for $Co_{0.2}$, $Co_{0.5}$, $Co_{0.8}$, and Co_3O_4 samples. The corresponding temperature ranges are 160–220 °C for $Co_{0.2}$ sample, 180–231 °C for $Co_{0.5}$ sample, 202–260 °C for $Co_{0.8}$ sample, and 283–313 °C for Co_3O_4 sample.

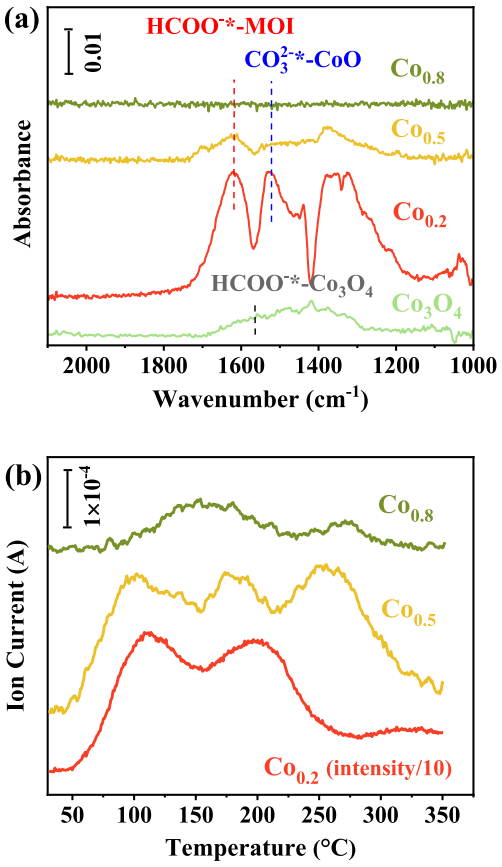

Fig. 6. (a) DRIFTS spectra during CO_2 + H_2 co-adsorption at 100 °C, revealing the presence of formate and carbonate species. (b) CO_2 desorption measured using TPD-MS (m/z = 44) from CO_2 + H_2 co-adsorption with a heating rate of 15 °C min^{-1}, and the intensities are normalized with He intensity.

To check the sample stability after high temperature reaction, the oxidation states of the samples after CO_2 hydrogenation were further investigated using XPS. We found that the Co fraction in the $Co_{0.2}$, $Co_{0.5}$, and $Co_{0.8}$ samples increased to 25%, 74%, and 86%, respectively (Fig. S9). Thus, the samples maintained the partial oxidation states and the Co fraction followed the same order as that of the fresh samples.

3.4. Surface reaction mechanisms

To understand the reason why the samples with higher CoO concentration have lower activation energy of CO_2 to CH_4 conversion, we analyzed the surface species recorded by DRIFTS in the operando experiment. The adsorbed species were identified according to our previous work on IR peak assignments and intermediates identification [17,18]. The assigned vibrations of the main IR peaks are listed in Table 2. As shown in Fig. 6(a), after CO_2 + H_2 co-adsorption, on the $Co_{0.2}$ surface we found formate located at the metal–oxide interface ($HCOO^{-}$*–MOI) and carbonate located on the oxide surface (CO_3^{2-}*–CoO); on the $Co_{0.5}$ surface, $HCOO^{-}$*–MOI was the main adsorption product; on the $Co_{0.8}$ surface, no visible adsorbed species was found; on Co_3O_4 surface, oxide-bound formate ($HCOO^{-}$*–Co_3O_4) was observed. The peaks with wavenumbers below 1500 cm^{-1} were not listed specifically, but they are the corresponding O–C–O symmetric and C–H bending modes according to our previous assignment [18]. The peak positions are very similar as those observed on Ru/Al_2O_3 in our previous work [18]. The formation of formate could originate from CO_2 interaction with the adsorbed H_2 on the under-coordinated cobalt atom on the interfacial CoO and/or on the metallic site of Co [34,35]; and the carbonate could be formed from CO_2 adsorption on the metal oxide surfaces [36,37]. The peak intensities of the adsorption species are the strongest on $Co_{0.2}$ sample, implying an enhanced amount of the adsorbed species on this sample. Moreover, while the formate species formed on all the sample surfaces, CO_3^{2-}*–CoO formed exclusively on the $Co_{0.2}$ surface. This suggests

Table 2
Activation energies of CH_4 formation ($E_a^f(CH_4)$), CO_2 desorption from CO_2 + H_2 co-adsorption ($E_a^{d1}(CO_2)$and $E_a^{d2}(CO_2)$), the main adsorption products on the sample surfaces and the corresponding main infrared peaks, i.e., O–C–O asymmetric stretching (ν_{as}(O–C–O)). $E_a^{d1}(CO_2)$and $E_a^{d2}(CO_2)$ refer to the first and second peak in the TPD spectrum, respectively.

Sample	$E_a^f(CH_4)$(kJ mol^{-1})	$E_a^{d1}(CO_2)$(kJ mol^{-1})	$E_a^{d2}(CO_2)$(kJ mol^{-1})	Main adsorption species	ν_{as}(O − C − O) (cm^{-1})
Co_3O_4	198.83 ± 0.74	N/A	N/A	$HCOO^{-}$*–Co_3O_4	1570
$Co_{0.2}$	91.21 ± 0.45	38.04 ± 3.08	76.09 ± 12.45	$HCOO^{-}$*–MOI; CO_3^{2-}*–CoO	1620; 1520
$Co_{0.5}$	107.47 ± 0.35	44.47 ± 4.02	129.17 ± 9.32	$HCOO^{-}$*–MOI	1620
$Co_{0.8}$	113.11 ± 157	–	–	–	–

that $Co_{0.2}$ sample might promote additional CO_2 adsorption via forming an additional chemisorption product on the CoO site.

To confirm the observations in IR, CO_2-TPD was performed. Fig. 6(b) shows the CO_2 desorption spectra (m/z = 44) of the three $Co_x(CoO)_{1-x}$ samples. The $Co_{0.2}$ TPD shows two peaks ~110 °C and 200 °C and a weak peak at ~320 °C; $Co_{0.5}$ shows three clear peaks at ~100 °C, 180 °C, and 260 °C respectively; $Co_{0.8}$ is different showing only two desorption peaks at ~160 °C, and 270 °C respectively. It is common that CO_2 desorbs at room temperature on metal oxide surfaces [38–42], while below 0 °C zero on metal surfaces [43–46]. Thus, these desorption peaks are ascribed to the CO_2 adsorbed on the CoO. With the increase of metallic cobalt fraction, the peak intensity of CO_2 desorption becomes weaker, indicating a decreasing amount of adsorbed CO_2.

Note that the desorption peak intensity on the $Co_{0.2}$ sample is more than ten-fold higher than that for the other samples. The intensity trend of the TPD measurements is consistent with the DRIFTS result of the CO_2 adsorption. However, the differences in the amount of CO_2 adsorbed on the three samples are much larger than the differences of their BET surface areas. While BET was measured using N_2 isotherm and reflects physisorption properties, CO_2 adsorption embodies chemisorption properties of the reactive surface, as CO_2 adsorption is used as an indicator of Lewis basicity of the surface [42,47,48]. Higher CO_2 adsorption capacity implies more adsorption sites, and stronger CO_2 binding implies more basic property of the surface. Therefore, the sample with more CoO component adsorbing more CO_2 further confirms that CoO acts as active sites for CO_2 adsorption. This also explains the exclusive existence of CO_3^{2-*}–CoO on the $Co_{0.2}$ sample observed in DRIFTS: more chemisorbed CO_2 increased the concentration of CO_3^{2-*} species on CoO sites via a CO_2-surface O combination.

We also checked the signals of H_2 and CH_4 from the TPD-MS measurement. As shown in Fig. S10, only very weak signals of H_2 were found and no observable CH_4 was produced. These phenomena hint that very limited amount of H_2 adsorbed on all these sample surfaces, and the hydrogenation of CO_2 either could not take place at this very low concentration of reactant gases or produced scanty products that below the detection limit.

The CO_2 binding energies were evaluated using the activation energies of CO_2 desorption, $E_a^d(CO_2)$ determined from TPD data at various heating rates (Table 2, Fig. S11) [49,50],

$$\ln\frac{T_p^2}{\kappa} = \ln\frac{E_a^d}{R} - \ln k_0 + \frac{E_a^d}{R\cdot T_p}$$

in which E_a^d is the activation energy of desorption, T_p is the maximal temperature of desorption, κ is the heating rate, R is the gas constant, and k_0 is a constant.

From the first desorption peak, we find $E_a^{d1}(CO_2)$ = 38 and 44 kJ mol^{-1} on $Co_{0.2}$ and $Co_{0.51}$ surfaces, respectively. $E_a^{d2}(CO_2)$, from the second desorption peak, = 76 and 129 kJ mol^{-1} on $Co_{0.2}$ and $Co_{0.5}$ surfaces, respectively. $E_a^d(CO_2)$ is not reported for the $Co_{0.8}$ sample due to the very weak desorption peaks and associated large uncertainty. The values of $E_a^{d1}(CO_2)$ and $E_a^{d2}(CO_2)$ are comparable to the reported CO_2 binding energies on pristine and defective metal oxide surfaces, respectively [51,52]. Therefore, we ascribe the low temperature desorption as originated from CO_2 adsorbed on the pristine CoO surface, which leads to similarly low activation energy of desorption on both $Co_{0.2}$ and $Co_{0.5}$ surfaces; the high temperature desorption as from CO_2 adsorbed on defective CoO surface, which leads to much stronger activation energy of desorption. The $E_a^{d2}(CO_2)$ on $Co_{0.2}$ sample is nearly twofold lower than that on $Co_{0.5}$ sample, suggesting a moderate adsorption of CO_2 on $Co_{0.2}$ surface compared to strong adsorption of CO_2 on $Co_{0.5}$ surface. As explained above, the stronger CO_2 binding indicates a stronger Lewis basic surface. Hence, the $Co_{0.5}$ surface is more basic than the $Co_{0.2}$ surface, probably due to a higher concentration of metallic cobalt of the $Co_{0.5}$ sample.

It is interesting that more CO_2 adsorbs on the $Co_{0.2}$ surface than on the $Co_{0.5}$ surface although the binding energy is actually larger for the $Co_{0.5}$ surface. We can understand this by noting that if we are below the desorption temperature, the capacity of the surface to adsorb CO_2 is related to the number of binding sites. Since $Co_{0.2}$ has more CoO sites, it can bind more CO_2.

The observation of enhanced adsorption of CO_2 on the $Co_{0.2}$ sample is sufficient to explain the improved catalytic performance of $Co_{0.2}$ because the adsorbed species might be byproducts rather than reaction intermediates. To check the reactivity of the adsorbed species, we analyzed the evolution of these adsorbed species using our previously developed method [18]. As shown in Fig. 7(a, b), $HCOO^{-*}$–MOI was reduced almost linearly upon heating on both $Co_{0.2}$ and $Co_{0.5}$ samples, indicating this species is a reaction intermediate. CO_3^{2-*}–CoO on $Co_{0.2}$ surface (Fig. 7(b)) and $HCOO^{-*}$–Co_3O_4 on Co_3O_4 surface (Fig. 7(c)) increased while heating, but started to decrease when CH_4 started to be formed. Thus, these two species were also reaction intermediates. Unfortunately, water produced in the reaction condensed on the windows and gave strong IR interference. We were only able to track the surface species up to 200 °C for $Co_{0.2}$ and $Co_{0.5}$ samples, and 320 °C for Co_3O_4 sample. However, Liu and the co-authors have proved using theoretical calculations that the wet surfaces favored the protonation of carbonate through interacting with the neighboring hydroxyl groups to form bicarbonate [36,37]. The bicarbonate is an intermediate of CH_4 formation from CO_2 hydrogenation reaction according to our previous work and the other report [17,53].

These results affirm that the adsorption of CO_2 has a positive effect on the CO_2 methanation reaction because all the adsorbed species are consumed. Better adsorption of CO_2 is related to an improved catalytic performance of the sample. This could also be the reason for the differences in the activation energies of CH_4 formation, where $E_a^f(CH_4)$ is the lowest on $Co_{0.2}$ sample. This further indicates that CO_2 adsorption step is the rate determining step of the overall hydrogenation reaction.

It is interesting to compare these results with our previous results for CO_2 methanation on Ru/Al_2O_3 [17,18]. There, CO_3^{2-*} and $HCOO^{-*}$ on the oxide site are byproducts, not reaction intermediates as they are here. This confirms our previous supposition of surface-structure sensitive reactivity of the adsorbed species.

3.5. Surface electronic structure

A further mechanistic investigation should reveal whether the CoO component of our catalysts participated the catalytic reaction. Considering that heterogeneous catalysis proceeds by electron transfer between the adsorbates and the surface atoms, we can get this information on the activity of CoO by measuring the valence band maximum (VBM) of the surface electronic states. For this measurement, we used a higher resolution XPS which did not allow us to transfer samples without air exposure. Thus, we transferred a $Co_{0.8}$ sample to the NAP-XPS system through air. This sample was then reduced at 350 °C with 0.4 mbar H_2 flow in the NAP-XPS sample preparation chamber. We used XPS core level spectra to determine the composition of the sample after transfer and after 1 h and 2 h of H_2 reduction (Fig. S12). After 2 h, the sample was fully reduced and we used this to provide standard core level and valence band spectra for Co for deconvolution with the CasaXPS software [26,54]. After 1 h, the sample was partially reduced with composition of 58% Co and 42% CoO. The core level spectrum of this partially reduced sample is shown in Fig. 8(a). A deconvoluted valence band spectrum is shown in Fig. 8(b).

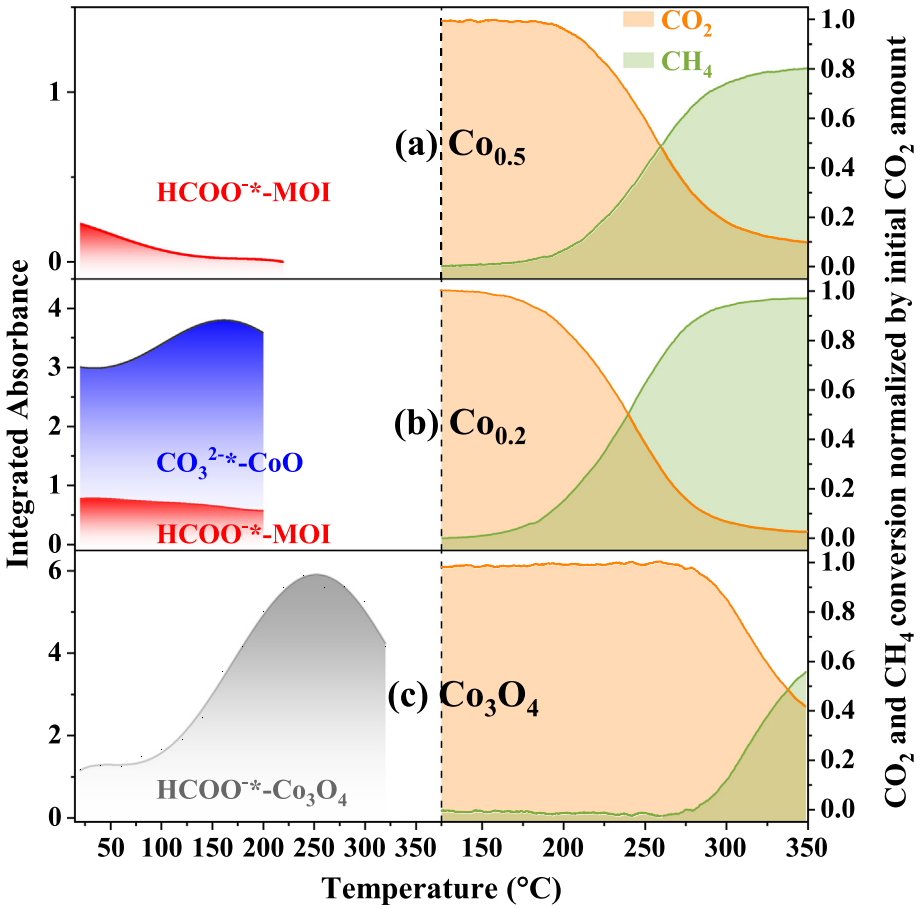

Fig. 7. The evolution of adsorbed species and CO_2 to CH_4 conversions during CO_2 hydrogenation on (a) $Co_{0.5}$, (b) $Co_{0.2}$, (c) Co_3O_4. Left panels were data from DRIFTS, and right panels were data from MS.

The fraction of Co from the valence band deconvolution is 47%, as compared to 58% from the core level deconvolution. The difference is not completely understood and may be related to differing surface sensitivity and/or to deconvolution error. The onset of the edge of the valence band for CoO is 1.15 eV below the Fermi level, as indicated by the line in Fig. 8(b). This value is so large that at the temperatures used in this work, it is not possible to thermally excite a sufficient number of electron hole pairs to produce catalytic activity. Although there is a "tail" extended to Fermi level, the population is very small compared to the abundantly electronic states of Co.

Therefore, we conclude that the CoO component does not contribute to the hydrogenation process. In contrast, the Co component has high electron density near the Fermi level, suggesting that the excited electrons for the hydrogenation steps are offered by Co. This is in line with the indication from CH_4 production rate per surface area discussed in Section 3.2 that the rate per surface area increased with the increasing concentration of Co. Species which are adsorbed on the CoO sites contribute to the catalysis through migration from CoO to the interfacial Co atoms. This is the same as that found on the on Ru/Al_2O_3 [17].

Here we envision that, when Co concentration decreased to a critical point, the hydrogenation will be suppressed because of the lack of electronically active center. We speculate this critical point is below 5 wt% (~6% molar concentration) referring to the research on Ru/Al_2O_3 catalysts where increasing Ru loading from 0.1 wt% to 5 wt% on Al_2O_3 facilitates the CH_4 yield and selectivity in CO_2 hydrogenation reaction [55]. However, the in situ phase change method here used would be improper to synthesize such low concentration of Co. Different synthetic method, such as chemical or physical deposition, could be applied for extending this investigation.

In addition, we noticed that the differences in the overall kinetics of CO_2 conversion (Fig. 4(d)) are smaller than those in the intensities of CO_2 adsorption/desorption (Fig. 6) on these samples. This could be understood that the samples with higher Co concentration could reduce the migration distance of the adsorbed species, and reserve more available electrons for the hydrogenation steps. These effects compensated partially the drawbacks of less CO_2 adsorption and reduced the differences in the overall kinetics of CO_2 conversion.

4. Conclusions

We have shown a facile method to synthesize "self-supported" cobalt nanoparticles composed of $Co_x(CoO)_{1-x}$ with different ratios of x= Co/(Co + CoO) via reduction of precursor Co_3O_4 nanoparticles in H_2 gas flow to investigate the relation between the metal/metal oxide fractions and their catalytic properties. Samples with the metal ratios of x= 0.2, 0.5 and 0.8 were obtained. The samples show very high activity in the Sabatier reaction. Super high conversions of CO_2 reach 98%, 99%, and 93% on $Co_{0.2}$, $Co_{0.5}$, and $Co_{0.8}$ samples, respectively at 350 °C, where the reaction meets the reaction thermodynamic limit. Below 280 °C, the activity varies with the sample in the order $Co_{0.2}$ > $Co_{0.5}$ > $Co_{0.8}$ > Co_3O_4 at all temperatures. For instance, 63%, 53%, and 23% CO_2 are converted at 250 °C on $Co_{0.2}$, $Co_{0.5}$, and $Co_{0.8}$ samples, respectively. The $Co_{0.2}$ sample even shows

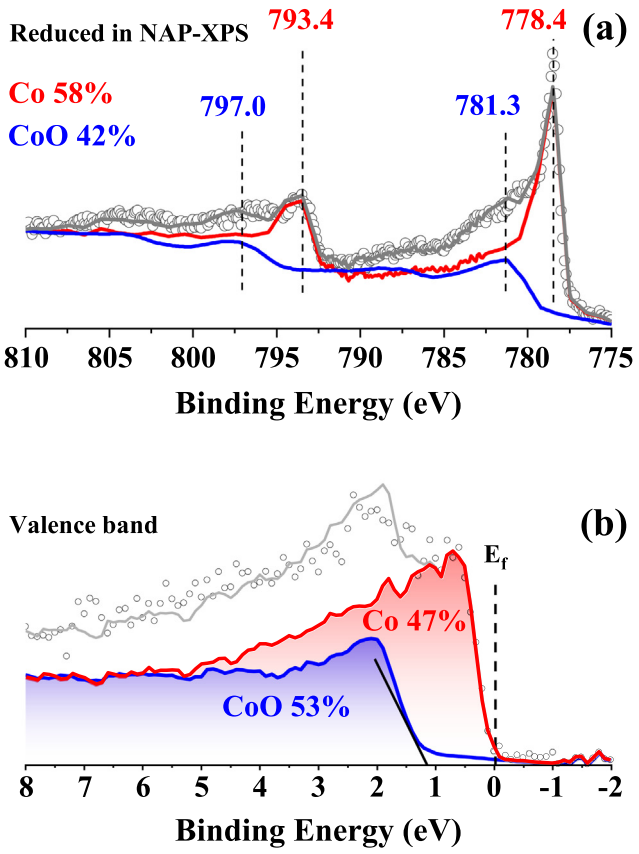

Fig. 8. (a) Core-level XPS and (b) valence band of the partially reduced sample (58% Co and 42% CoO) prepared and measured in NAP-XPS. The black line which is crossed at 1.15 eV of x-axis shows the onset of the edge of the valence band of CoO. Fermi level (E_f) is at 0 eV.

low-temperature activities from 160 to 180 °C, at which temperatures the rest samples do not have activities. The overall activation energy of CH_4 formation increases with the sample in the sequence of $Co_{0.2}$ < $Co_{0.5}$ < $Co_{0.8}$ < Co_3O_4. Therefore, there is an optimal composition of metal and metal oxide in the catalyst to achieve the highest reactivity.

The differences in reactivity among the samples originate from the different functions of the metal and the metal oxide. CoO provides active sites of CO_2 adsorption but not electron-transfer sites for the hydrogenation reaction. Co acts as an electronically active center for the hydrogenation reaction. The derivative adsorbed products are observed as formate and carbonate, and these are found to be intermediates of CH_4 formation. Of the partially reduced samples, the $Co_{0.2}$ sample has highest CoO concentration; consequently it adsorbs the largest amount of CO_2. Moreover, the low fraction of Co/(Co + CoO) facilitates moderate binding of CO_2. The CO_2 adsorption step could be the rate-determining step of the overall methanation reaction. Therefore, the $Co_{0.2}$ sample shows the highest reactivity: the lowest onset temperature and activation energy of CH_4 formation, and the highest conversion of CO_2 below thermodynamic limit. In comparison, the $Co_{0.5}$ sample with its higher fraction of Co/(Co + CoO) has a higher binding energy for CO_2 due to its stronger Lewis basicity; but it adsorbs less CO_2 because there are less CoO sites. As a result, the $Co_{0.5}$ sample converts less CO_2 than the $Co_{0.2}$ sample. $Co_{0.8}$ sample does not have the advantage of abundant CoO concentration, therefore not show significant CO_2 adsorption amount. This leads to the lowest reactivity of $Co_{0.8}$ compared to $Co_{0.2}$ and $Co_{0.5}$ samples.

These results of this work elucidate the optimal composition of metal and metal oxide for achieving the highest catalytic reactivity in the Sabatier reaction. Furthermore, they clarified the different active functions of the metal and metal oxide in the whole CO_2 hydrogenation reaction. These two main attainments open the way for the design of efficient catalysts with the optimal ratio of metal over metal oxide.

Declaration of Competing Interest

The authors declare that they have no known competing financial interests or personal relationships that could have appeared to influence the work reported in this paper.

Acknowledgments

SCCER HeE, which is financially supported by Innosuisse, the Swiss Innovation Agency, is gratefully acknowledged. The NAP-XPS system is funded by the SNSF R'EQUIP project (No. 170736). W.L. acknowledges the financial support from SNSF (Ambizione Project PZ00P2_179989). M.L would like to thank the China Scholarship Council for the PhD grant (Grant No. 201506060156). K.Z highly acknowledges Daniel Auerbach for his enormous help in revising the writing. We also thank Bardiya Valizadeh and Arunraj Chidambaram from Laboratory of Molecular Simulation (LSMO), EPFL for the help in BET measurement.

Appendix A. Supplementary data

Supplementary data to this article can be found online at https://doi.org/10.1016/j.jechem.2020.05.025.

References

[1] J. Artz, T.E. Müller, K. Thenert, J. Kleinekorte, R. Meys, A. Sternberg, A. Bardow, W. Leitner, Chem. Rev. 118 (2018) 434–504.
[2] W. Li, H. Wang, X. Jiang, J. Zhu, Z. Liu, X. Guo, C. Song, RSC Adv. 8 (2018) 7651–7669.
[3] R. Mutschler, E. Moioli, W. Luo, N. Gallandat, A. Züttel, J. Catal. 366 (2018) 139–149.
[4] F. Marques Mota, D.H. Kim, Chem. Soc. Rev. 48 (2019) 205–259.
[5] E. Moioli, A. Züttel, Sustain. Energy Fuels 4 (2020) 1396–1408.
[6] R.W. Dorner, D.R. Hardy, F.W. Williams, H.D. Willauer, Energy Environ. Sci. 3 (2010) 884–890.
[7] E.V. Kondratenko, G. Mul, J. Baltrusaitis, G.O. Larrazabal, J. Perez-Ramirez, Energy Environ. Sci. 6 (2013) 3112–3135.
[8] I.A. Fisher, A.T. Bell, J. Catal. 172 (1997) 222–237.
[9] I.A. Fisher, A.T. Bell, J. Catal. 178 (1998) 153–173.
[10] X.-M. Liu, G.Q. Lu, Z.-F. Yan, J. Beltramini, Ind. Eng. Chem. Res. 42 (2003) 6518–6530.
[11] S. Kattel, B. Yan, Y. Yang, J.G. Chen, P. Liu, J. Am. Chem. Soc. 138 (2016) 12440–12450.
[12] S. Kattel, P.J. Ramírez, J.G. Chen, J.A. Rodriguez, P. Liu, Science 355 (2017) 1296–1299.
[13] T. Chen, J. Su, Z. Zhang, C. Cao, X. Wang, R. Si, X. Liu, B. Shi, J. Xu, Y.-F. Han, ACS Catal. 8 (2018) 8606–8617.
[14] G. Melaet, W.T. Ralston, C.-S. Li, S. Alayoglu, K. An, N. Musselwhite, B. Kalkan, G.A. Somorjai, J. Am. Chem. Soc. 136 (2014) 2260–2263.
[15] A. Boffa, C. Lin, A.T. Bell, G.A. Somorjai, J. Catal. 149 (1994) 149–158.
[16] G. Prieto, M.I.S. De Mello, P. Concepción, R. Murciano, S.B.C. Pergher, A. Martínez, ACS Catal. 5 (2015) 3323–3335.
[17] K. Zhao, L. Wang, M. Calizzi, E. Moioli, A. Züttel, J. Phys. Chem. C 122 (2018) 20888–20893.
[18] K. Zhao, L. Wang, E. Moioli, M. Calizzi, A. Züttel, J. Phys. Chem. C 123 (2019) 8785–8792.
[19] S. Yoon, K. Oh, F. Liu, J.H. Seo, G.A. Somorjai, J.H. Lee, K. An, ACS Catal. 8 (2018) 5391–5398.
[20] C.K. Vance, C.H. Bartholomew, Appl. Catal. 7 (1983) 169–177.
[21] S. Kattel, W. Yu, X. Yang, B. Yan, Y. Huang, W. Wan, P. Liu, J.G. Chen, Angew. Chem. 55 (2016) 7968–7973.
[22] S. Kuld, M. Thorhauge, H. Falsig, C.F. Elkjær, S. Helveg, I. Chorkendorff, J. Sehested, Science 352 (2016) 969.
[23] K. Zhao, J. Zhang, W. Luo, E. Moioli, M. Spodaryk, A. Züttel, submitted, (2020).
[24] A.M. Karim, Y. Su, M.H. Engelhard, D.L. King, Y. Wang, ACS Catal. 1 (2011) 279–286.

[25] K.C. Sabat, R.K. Paramguru, S. Pradhan, B.K. Mishra, Plasma Chem. Plasma Process 35 (2015) 387–399.
[26] W. Luo, S. Zafeiratos, J. Phys. Chem. C 120 (2016) 14130–14139.
[27] L.J. Garces, B. Hincapie, R. Zerger, S.L. Suib, J. Phys. Chem. C 119 (2015) 5484–5490.
[28] G. Garbarino, D. Bellotti, P. Riani, L. Magistri, G. Busca, Inter. J. Hydrog, Energy 40 (2015) 9171–9182.
[29] G. Garbarino, D. Bellotti, E. Finocchio, L. Magistri, G. Busca, Catal. Today 277 (2016) 21–28.
[30] M.S. Duyar, A. Ramachandran, C. Wang, R.J. Farrauto, J. CO2 Util. 12 (2015) 27–33.
[31] G.D. Weatherbee, C.H. Bartholomew, J. Catal. 77 (1982) 460–472.
[32] A. Karelovic, P. Ruiz, ACS Catal. 3 (2013) 2799–2812.
[33] G.L. Bezemer, J.H. Bitter, H.P.C.E. Kuipers, H. Oosterbeek, J.E. Holewijn, X. Xu, F. Kapteijn, A.J. van Dillen, K.P. de Jong, J. Am. Chem. Soc. 128 (2006) 3956–3964.
[34] Y. Pan, D. Mei, C. Liu, Q. Ge, J. Phys. Chem. C 115 (2011) 10140–10146.
[35] S. Kato, S.K. Matam, P. Kerger, L. Bernard, C. Battaglia, D. Vogel, M. Rohwerder, A. Züttel, Angew. Chem. 55 (2016) 1–6.
[36] Y. Pan, C. Liu, Q. Ge, Langmuir 24 (2008) 12410–12419.
[37] Y. Pan, C. Liu, D. Mei, Q. Ge, Langmuir 26 (2010) 5551–5558.
[38] O. Seiferth, K. Wolter, B. Dillmann, G. Klivenyi, H.J. Freund, D. Scarano, A. Zecchina, Surf. Sci. 421 (1999) 176–190.
[39] A. Hakim, T.S. Marliza, N.M. Abu Tahari, R.W.N. Wan Isahak, R.M. Yusop, W. M. Mohamed Hisham, A.M. Yarmo, Ind. Eng. Chem. Res. 55 (2016) 7888–7897.
[40] G. Krenn, J. Schoiswohl, S. Surnev, F.P. Netzer, R. Schennach, Top Catal. 46 (2007) 231–238.
[41] R. Bal, B.B. Tope, T.K. Das, S.G. Hegde, S. Sivasanker, J. Catal. 204 (2001) 358–363.
[42] K. Pokrovski, K.T. Jung, A.T. Bell, Langmuir 17 (2001) 4297–4303.
[43] J. Wang, B. Hokkanen, U. Burghaus, Surf. Sci. 577 (2005) 158–166.
[44] S. Wohlrab, D. Ehrlich, J. Wambach, H. Kuhlenbeck, H.-J. Freund, Surf. Sci. 220 (1989) 243–252.
[45] H.J. Freund, H. Behner, B. Bartos, G. Wedler, H. Kuhlenbeck, M. Neumann, Surf. Sci. 180 (1987) 550–564.
[46] J. Wambach, G. Illing, H.J. Freund, Chem. Phys. Lett. 184 (1991) 239–244.
[47] W.N.R.W. Isahak, Z.A.C. Ramli, M.W. Ismail, K. Ismail, R.M. Yusop, M.W.M. Hisham, M.A. Yarmo, J. CO2 Util. 2 (2013) 8–15.
[48] P. Kuśtrowski, L. Chmielarz, E. Bożek, M. Sawalha, F. Roessner, Mater. Res. Bull. 39 (2004) 263–281.
[49] H.E. Kissinger, Anal. Chem. 29 (1957) 1702–1706.
[50] G. Munteanu, E. Segal, Thermochimica. Acta 89 (1985) 187–194.
[51] U. Burghaus, Prog. Surf. Sci. 89 (2014) 161–217.
[52] U. Burghaus, in: New and Future Developments in Catalysis, Elsevier, Amsterdam, 2013, pp. 27–47.
[53] M. Marwood, R. Doepper, A. Renken, Appl. Catal. A: General 151 (1997) 223–246.
[54] V.A. Saveleva, L. Wang, W. Luo, S. Zafeiratos, C. Ulhaq-Bouillet, A.S. Gago, K.A. Friedrich, E.R. Savinova, J. Phys. Chem. Lett. 7 (2016) 3240–3245.
[55] J.H. Kwak, L. Kovarik, J. Szanyi, ACS Catal. 3 (2013) 2449–2455.